Water structure as a function of temperature from X-ray scattering experiments and *ab initio* molecular dynamics

Greg Hura,[a] **Daniela Russo,**[b] **Robert M. Glaeser,**[ac] **Teresa Head-Gordon,**[*ab]
Matthias Krack[d] **and Michele Parrinello**[e]

[a] *Graduate Group in Biophysics, University of California, Berkeley, CA 94720, USA*
[b] *Department of Bioengineering, University of California, Donner 459A, Berkeley, CA 94720, USA*
[c] *Department of Molecular and Cell Biology, University of California, Berkeley, CA 94720, USA*
[d] *Swiss Center for Scientific Computing, Via Cantonale, CH-6928, Manno, Switzerland*
[e] *ETH Zurich, Physical Chemistry, Hoenggerberg-HCI, CH-8093, Zurich, Switzerland*

We present high-quality X-ray scattering experiments on pure water taken over a temperature range of 2 to 77 °C using a synchrotron beam line at the advanced light source (ALS) at Lawrence Berkeley National Laboratory. The ALS X-ray scattering intensities are *qualitatively* different in trend of maximum intensity over this temperature range compared to older X-ray experiments. While the common procedure is to report both the intensity curve and radial distribution function(s), the proper extraction of the real-space pair correlation functions from the experimental scattering is very difficult due to uncertainty introduced in the experimental corrections, the proper weighting of OO, OH, and HH contributions, and numerical problems of Fourier transforming truncated data in Q-space. Instead, we consider the direct calculation of X-ray scattering spectra using electron densities derived from density functional theory based on real-space configurations generated with classical water models. The simulation of the experimental intensity is therefore definitive for determining radial distribution functions over a smaller Q-range. We find that the TIP4P, TIP5P and polarizable TIP4P-Pol2 water models, with DFT-LDA densities, show very good agreement with the experimental intensities, and TIP4P-Pol2 in particular shows quantitative agreement over the full temperature range. The resulting radial distribution functions from TIP4P-Pol2 provide the current best benchmarks for real-space water structure over the biologically relevant temperature range studied here.

Introduction

Liquid water structure is characterized by X-ray (or neutron) diffraction that measures experimental intensities as a function of momentum transfer, $Q = 4\pi\sin(\theta/2)/\lambda$, where λ is the wavelength and θ is the scattering angle with respect to the incident beam. The most recent X-ray data taken at ambient conditions at the advanced light source (ALS) at Lawrence Berkeley National Laboratory exhibited significant differences when compared to the scattering curves of past X-ray experiments.[1–3] We believe the new measurements to be superior since they benefit from the use of a third generation synchrotron source, more accurate intensities using a modern CCD detector, and careful control of error in the applied corrections.[3] However, no such high quality X-ray measurements exist yet at other thermodynamic state points. In this study we detail the collection and processing of X-ray diffraction intensity data from pure liquid water throughout the temperature range of 2 to 77 °C at ambient pressure, a temperature range that is most important for water related to biological studies.

The intensity is the true experimental observable in which error-bars are well-defined. However, it is typical practice for water scattering experiments to also report radial distribution functions in addition to the intensity profile, primarily because it is more convenient and practical to consider water structure in terms of real-space distribution functions.[1,4–14] In actuality,

the oxygen–oxygen radial distribution function, $g_{OO}(r)$, extracted from the X-ray diffraction measurements are highly-derived functions, not necessarily unique, and there is no way of quantifying the errors introduced in their extraction based on finite Q data.[3] Therefore it is not surprising that the $g_{OO}(r)$ obtained by various X-ray and neutron scattering groups over the last 30 years has been inconsistent.[4,10,12] Recently, independent experimental approaches of X-ray[1] and neutron[14] scattering, using different analyses to extract radial distribution functions,[2,15] independently converged on the same oxygen–oxygen radial distribution function for ambient temperature and pressure as shown in Fig. 1.

However, extracting real-space pair correlation functions from the intensity remains a primary source of uncertainty that potentially degrades the actual high quality of the experimental data itself. Currently it is thought that collecting the intensity out to $Q = 20$–25 Å^{-1} would be needed to reliably Fourier transform the data to get converged real-space functions. Based on the uncertainties in any approach for extracting real-space functions, such as Q-space continuation,[7] fitting procedures in r-space,[2] and reverse Monte Carlo methods[16,17] and its extensions,[15] it is important to further test the assumptions made in deriving radial distribution functions based on a smaller range of Q. With the advent of completely *ab initio* simulations of liquid water,[18–21] it is now possible to predict the X-ray scattering from the distribution of electron density, $\rho(\mathbf{r})$, generated from the condensed phase simulation trajectory[22] using eqn. (1)

DOI: 10.1039/b301481a

Phys. Chem. Chem. Phys., 2003, **5**, 1981–1991 **1981**
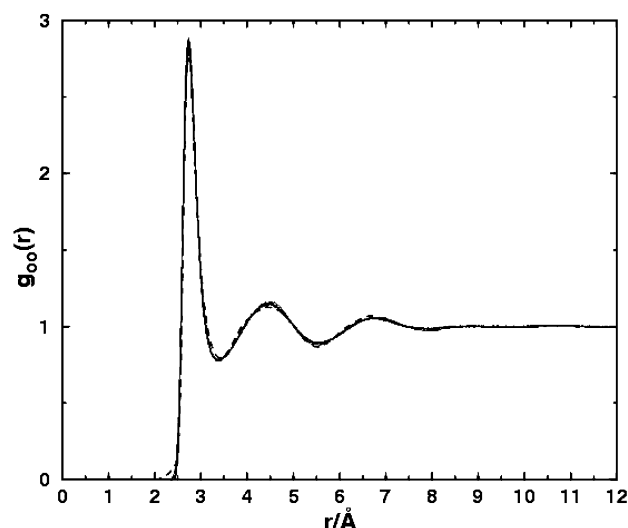
Fig. 1 Comparison of $g_{OO}(r)$ derived from r-space fitting using ALS experimental data[2] (dashed line) and neutron experimental data and empirical potential structural refinement (black line).[14]

$$I(Q) = \left\langle |F(Q)|^2 \right\rangle \quad \text{with } F(Q) = \int_0^\infty \rho(r)\exp(iQr)dr \quad (1)$$

This allows for the straight simulation of the true experimental observable, the intensity, without requiring the contrived and error-prone process of extracting radial distribution functions from intensity data over a finite Q-range. If the simulated intensity curve using eqn. (1) agrees well with experiment (with only moderately large Q-ranges), then we can analyze the corresponding real-space trajectory to ascertain the pair distribution function(s).

In this study we consider the direct calculation of X-ray scattering spectra using *ab initio* density functional theory with the LDA functional over the temperature range studied by experiment. The generation of the real-space "snapshots" could come from either a first principles molecular dynamics calculation,[18] that describes the time-evolution of the electronic structure, or a classical molecular dynamics simulation based on an empirical water model. Due to the current expense of simulating the full *ab initio* trajectory, we instead evaluate eqn. (1) by integrating over positions generated by the classical simulation of various water models.

The combined experimental and theoretical benchmarks are applied to judging the quality of various TIP non-polarizable[23,24] and polarizable[25] water force fields over the range of temperature of 2–77 °C that we have examined. We find that the TIP5P non-polarizable water model[24] and the TIP4P-Pol2[25] polarizable model, with DFT-LDA densities, show very good agreement with the experimental intensities, and TIP4P-Pol2 in particular shows quantitative agreement over the full temperature range. The resulting radial distribution functions from TIP4P-Pol2, and for TIP5P for temperatures greater than 25 °C, provide the current best benchmarks for real-space water structure over the biologically relevant temperature range studied here. We also examine the relative error introduced by LDA electron densities *vs.* error in water force field configurations, using an independent analysis method described in ref. 2 and 3.

Experimental methods

Experimental setup

The data collection was performed at the advanced light source (ALS) at Lawrence Berkeley National Laboratory on beam line 7.3.3. Doubly distilled and degassed water was used

Table 1 Specification of data collection for three different positions of the detector relative to the sample

| Position	Collection time/s	Detector center to sample holder distance/cm	Angle between X-ray beam and detector face normal	Q range/Å^{-1}
1	200	9.523	21.654°	0.1–5.6
2	300	8.532	53.501°	3.1–8.6
3	400	7.717	86.893°	6.4–11.1

in each experiment, and several data sets with independent fillings of the sample holder were collected at each temperature (2 °C, 11 °C, 22 °C, 33 °C, 44 °C, 55 °C, 66 °C, and 77 °C). A silicon monochromoter was used to produce an X-ray beam with spot size on the order of 100 μm, with 99% of the energy at 12.800 ± 0.001 keV or a wavelength of 0.9686 Å. This wavelength provided the best compromise between sufficient flux and maximizing our accessible Q-range. Data sets were collected with a flat slab water sample using a transmisson geometry, with the sample tilted with respect to the incoming X-ray beam by an angle of 30°.

A Bruker charge coupled device (CCD) area detector, mounted on a Huber diffractometer and with dimensions of 9.6×9.6 cm collected the diffracted X-rays. In order to realize the full range of 0.1 Å^{-1} < Q < 11.1 Å^{-1} provided in this study, the data were collected with the detector in three different positions which were pieced together for the final result. The sample to detector positions were determined to 100 μm precision while the angle between the X-ray beam and the normal to detector face were characterized on the order of mrads. The geometries at each detector position were determined by collecting PbS powder patterns with the powder placed within the sample holder and fitting the resulting sharp Bragg rings to determine all the geometric parameters. A more detailed description of this procedure can be found in previous work.[1] The three sample to detector positions and collection times are detailed in Table 1. The lowest angles were limited by the beam stop at 0.8832° or a $Q = 0.1$ Å^{-1}, the highest angles were limited by the monochromoter housing and sample holder aperture at 118° or at a $Q = 11.1$ Å^{-1}.

Our sample holder was based on a similar design of our previously described sample holder[1] with several additions in order to control the temperature of the sample, and is shown in Fig. 2 and described in the figure caption. Temperature control of the sample relied on a Peltier device or thermoelectric cooler. A thermocouple placed within the sample chamber, monitored the temperature. An Alpha Omega Instruments Series 800 Controller acted as the thermostat. One face of the Peltier device was placed in thermal contact with the aluminum plate augmented by a zinc oxide thermal grease. In order to achieve temperatures below room temperature a water cooled aluminum block was placed on the other side of the Peltier device as a heat sink. In order to prevent condensation below the dew point a helium shroud was built around the sample holder. The entrance and exit windows of the helium shroud were made of 1 μm thick Mylar purchased from Goodfellow Inc.

Experimental corrections

The collected raw intensity data were transformed to a circularly integrated scattering cross-section on a per electron scale versus Q. The following divides the corrections into two parts. The first deals with corrections that must be applied generally to all detector positions such as absorption, geometric corrections, and polarization of the radiation. The second set of corrections deals with overlapping data from different panels
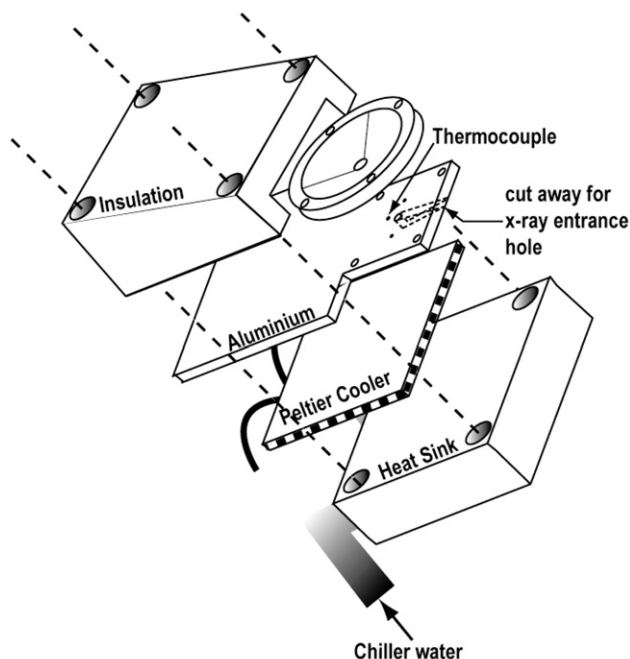
Fig. 2 Details of sample holder design. The sample was held in a cavity between a disc shape transparent Lucite plate and a heat conducting rectangular aluminum plate, and sealed together by a fitted rubber gasket. Each plate had a 3.0 mm hole drilled through them for the X-ray beam. The aluminum plate was fitted with inlet and outlet tubes so that water could fill the sample chamber after assembly, and a groove cut into it that allowed X-rays through the hole when the sample holder was tilted by 30° with respect to the X-ray beam. The Lucite plate had a 120° cone shaped tapered hole on its exiting face so as not to obstruct scattered X-rays. The 3 mm holes were sealed with 38 μm thick kapton (polyimide) window on the inward faces of the plates, in contact with the sample. The sample chamber was machined to nominally 500 μm thickness but the actual thickness varied depending on the filling and was at times thicker, presumably due to the bowing of the kapton windows.

and thus the contribution of background and sample holder scattering.

Corrections to the intensities due to absorption by air, water, and window material are given in the form

$$\frac{I}{I_0} = \left[\exp\left(\frac{-\mu_\rho t}{\sin \tau}\right) - \exp\left(\frac{-\mu_\rho t}{\nu}\right) \frac{\nu \sin \tau}{\mu_\rho (\sin \tau - \nu)} \right] \quad (2)$$

where I_0 is the intensity if there were no absorption in the sample, I is the measured intensity, t is the thickness, τ is the angle between the plane of the sample and the incident X-ray beam, and ν has the form $\nu = \cos\theta \, \sin\tau + \sin\theta \, \cos\phi \, \cos\tau$. The absorption coefficients, μ_ρ, can be obtained from http://www-cxro.lbl.gov/optical_constants using a tabulated format based on ref. 26. The absorption coefficient for water is 2.396 cm^2 g^{-1} for 1 °C water at our operating wavelength and varies proportionally with the density for different temperatures. The thicknesses of samples were determined by measuring the X-ray transmisson through the sample using a PIN diode. The error in the thickness was on the order of 0.02 cm and did not contribute significantly to the error of the intensity curve.

When the incident radiation is plane-polarized as in our experiment, the in-plane and out-of-plane polarization is treated separately, and the measured intensities must be re-scaled by the factor

$$P = P_{\text{in-plane}}[1 - (\sin\phi \, \sin\theta)^2] + P_{\text{out-plane}}[1 - (\cos\phi \, \sin\theta)^2] \quad (3)$$

where $P_{\text{in-plane}}$ and $P_{\text{out-plane}}$ are the fractional polarizations of the beam in the plane and out of the plane of the circulating electrons, respectively.

The data were also corrected for the $1/r^2$ fall off of intensity, and correction for pixel orientation with respect to the incident radiation. We discovered that detector manufacturers attempt to provide a correction of this sort in their bundled software for data read-out. Corrections to the image collected by the CCD includes distortions introduced by the fiber optic tapers connecting the plate to the chip, a dark current correction that takes into account photoelectrons ejected by thermal motions in the CCDs and any low-level background radiation in the experimental hutch, and finally a flat field correction that provides a correction for variations in pixel sensitivity. This correction involves a calibration measurement that collects a reference image intensity using either a radioactive source or scattering from a fluorescent material at a set distance from the detector. The image is used to generate a scale factor for each pixel such that, when applied to the flat field image, each pixel measures the same intensity. The set distance with which this correction is calibrated varies among manufacturers. If the calibration experiment involves a relatively small source to detector distance, then the geometric corrections ($1/r^2$ fall off, pixel orientation) are implicitly taken into account by the manufacturer in the flat field correction. This is the case for the Bruker detector, so we need to "uncorrect" the collected image for the manufacturers' geometry, and re-apply the correct geometric corrections for our experiment. This is an insidious problem since these detector corrections are applied before the "raw image" is available to the experimentalist, and the correction is not documented in the manufacturer's literature.

We next turn to the procedure for the subtraction of background that is required in order to match segments of the intensity over the full range of Q in this experiment. Fig. 3a shows the fully corrected, filled and empty sample holder data at one temperature, at a point before the three separate positions of the detector have been pieced together. We had intended to use the overlapping regions of the curves to determine an internal scale factor that would place all three segments of the data on the same scale. This is easily done for overlapping the second and third detector positions. However while the overlap between the first and second detector positions for the filled sample is quite good, the overlap between the first and second detector positions for the background is very poor. We attribute this mismatch to additional air-scattering by the X-ray beam once it exits the sample, something that is less of a problem for the filled sample because of its greater absorption cross-section. As a result, we could not simply overlap panels for the filled sample, overlap panels for the empty cell, and subtract the latter from the former to provide a correction for scattering background.

Instead, the background can be subtracted from the first detector position by making use of the prominent kapton window peak at $Q = 0.4$ Å^{-1} which occurs in a region where there are no sharp features in the liquid water scattering. The factor required for the background subtraction is found when the kapton peak is clearly removed and the intensity in the associated Q region is flat. This factor can be empirically fine-tuned by extrapolating the intensity to the value of the isothermal compressibility at $Q = 0$, once the intensity is on an electron units scale. In order to overlap the second panel with the first panel, two scale factors need to be found; a factor related to the flux over the exposure time (a_1) and a scaling for the kapton subtraction (a_2). This is summarized in eqn. (4)

$$a_1 I_2(Q) - a_2 I_k(Q) = I_1(Q) \quad (4)$$

where $I_2(Q)$ is the intensity of the filled sample holder in the second detector position, $I_k(Q)$ is the intensity of the background (empty cell), and $I_1(Q)$ is the intensity of the filled
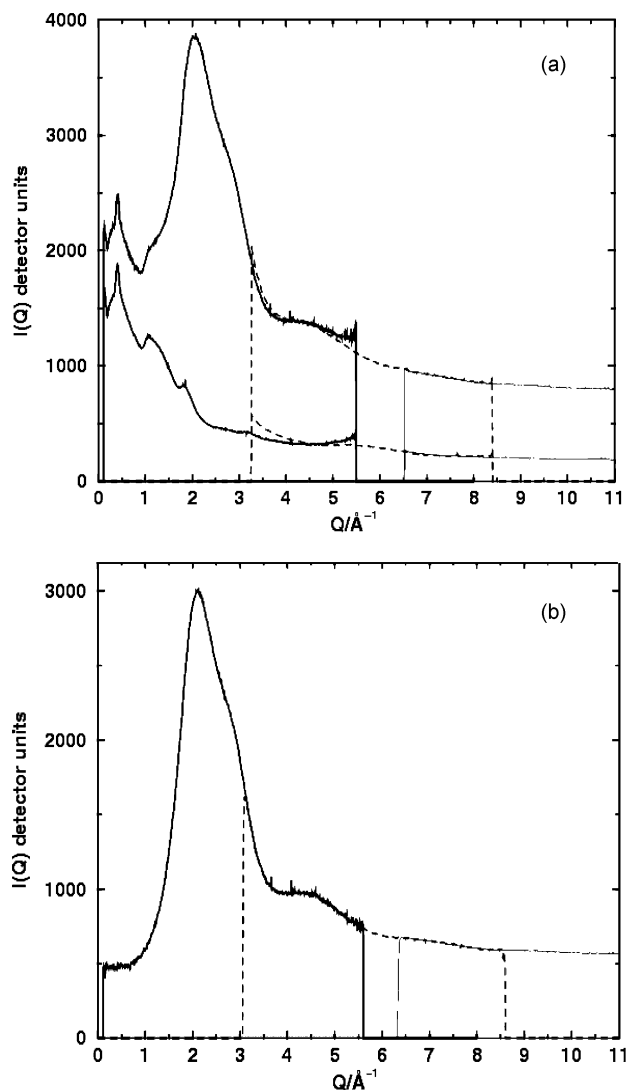
Fig. 3 (a) Fully corrected, filled and empty sample holder intensity data before the three separate positions of the detector have been pieced together. (b) The total intensity curve for filled and empty sample holder after piecing together.

sample holder in the first detector position. These two factors are determined by standard least-squares fitting over the overlapping Q range. The third detector position that already overlapped in shape with the second detector position used the same kapton subtraction factor, a_2. The resulting curve is shown in Fig. 3b.

Once we have the intensity curve over the full Q-range, we make a correction for inelastic or Compton scattering as discussed in ref. 1 using a fit to CISD calculations available for water.[27,28] The Krogh–Moe,[29,30] method was used to normalize the scattering intensity to an absolute scale.

Theoretical methods

It is conventional in the analysis of the scattering from molecular liquids to separate the intensity into contributions from individual molecules (self-scattering), and that arising from intermolecular correlations defined by the structure factor, $H(Q)$.

$$I(Q) = \sum_{ij} x_i x_j f_i(Q) f_j(Q) \frac{\sin Qr_{ij}}{Qr_{ij}} + \sum_{i \leq j} x_i x_j f_i(Q) f_j(Q) H_{ij}(Q) \quad (5)$$

where the sums are over the atom types present in the sample, x_i is the atomic fraction and $f_i(Q)$ the Q-dependent atomic scattering factor,[31] for atom type i. The structure factor is

$$H_{ij}(Q) = 4\pi\rho \int_0^\infty r^2 \mathrm{d}r [g_{ij}(r) - 1] \frac{\sin Qr}{Qr} \quad (6)$$

where ρ is the atomic density, r_{ij} are the intramolecular distances between atom centers, and $g_{ij}(r)$ is the radial distribution function describing intermolecular correlations between atom types i and j. In the case of X-rays the assumption is commonly made that the scattering can be represented as arising from independent neutral atoms, each with a spherical electron density distribution. However, it is clear from our previous work that a superposition of spherical electron densities of free atoms centered on the individual atoms of chemically bonded water is not adequately representative of the true charge distribution.[2]

We have recently introduced a modification of the atomic scattering factors for liquid water which re-scales them properly at low Q where chemical bonding effects are known to be significant, while retaining their values at large Q where chemical bonding effects on the core electron distribution should be negligible.[2] The modified atomic form factor (MAFF) $f'(Q)$ is of the form

$$f'(Q) = [1 + (\alpha - 1)\exp(-Q^2/2\delta^2)]f(Q) \quad (7)$$

where $f(Q)$ is the atomic scattering factor for the isolated atom, α is a scaling factor giving the redistribution of charge, and δ is a parameter to be fit, representing the extent of valence-electron delocalization induced by chemical bonding.[2] For liquid water we choose α to be 2.8 D, and the unknown parameter δ was fit by requiring the Debye expression curve to agree with the *ab initio* CI results for gas phase water.[28] Fig. 4 shows the difference in a simulated intensity when using the same partial structure factors [$h_{OO}(Q)$, $h_{OH}(Q)$, and $h_{HH}(Q)$] but free atom form factors based on isolated atoms or the MAFFs that take into account chemical bonding. The difference arises because of chemical bonding effects, which now weight the O–O terms as ∼85% of the signal, while O–H terms contribute ∼15%, with negligible contribution from H–H correlations.

Explicit quantum treatments of electronic structure in aqueous simulations have been reported, where all have relied
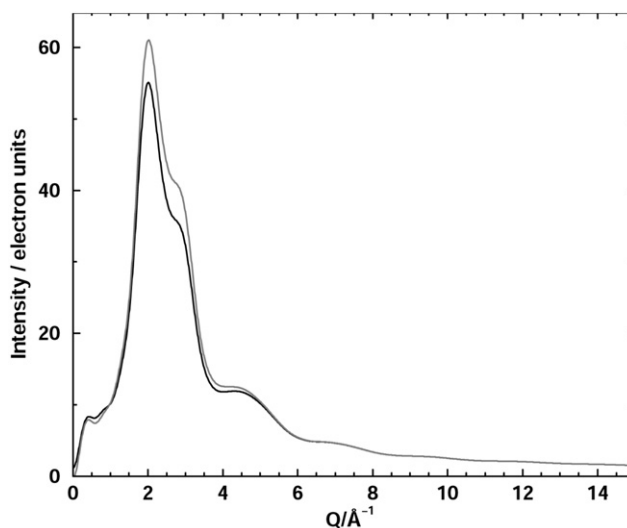
Fig. 4 The difference in simulated intensity when using the same partial structure factors [$h_{OO}(Q)$, $h_{OH}(Q)$, and $h_{HH}(Q)$] but free atom form factors based on isolated atoms (black line) or the MAFFs (gray line) that take into account chemical bonding.
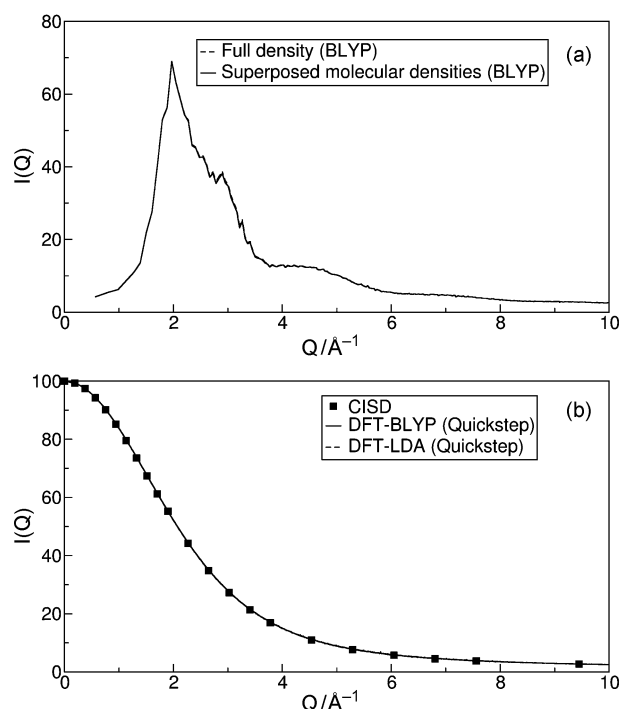
Fig. 5 (a) Coherent X-ray scattering intensities for liquid water calculated with Quickstep from a CPMD simulation of 64 water molecules using the full electronic density (dashed line) and a superposition of molecular densities (solid line). (b) Coherent X-ray scattering intensities of an isolated water molecule calculated with Quickstep using the functionals BLYP (solid line) and LDA (dashed line) compared with the intensities from a CISD calculation (squares).

on a local density approximation to density functional theory.[18–21,32] The cost of these calculations rises as N^3 where N is the number of basis functions or plane waves per atom, with a large coefficient relative to classical simulations that make these approaches computationally demanding, but potentially more predictive. Differences among functionals in the condensed phase have been investigated for liquid water in ref. 19, and commonly used functionals include BLYP[33–35] and PBE.[36] In principle, these approaches provide the current best theoretical means for providing intensity curves directly. These calculations can also be corrected for quantum effects.

As discussed in ref. 22, a direct calculation of the coherent X-ray scattering spectrum of liquid water by means of DFT is feasible when using an implementation of the Gaussian augmented plane wave (GAPW) method,[37] called Quickstep, which can perform all-electron *ab-initio* DFT calculations for periodic systems.[38] The evaluation of an intensity curve from a 10-ps-long CPMD simulation of 64 water molecules with the gradient-corrected BLYP functional and with an average ionic temperature of 318 K (ref. 20) using the full electronic charge distributions was compared to the ALS2000 experiment,[1] which was conducted at room temperature. Overall these results are promising, but are not in themselves definitive because of the short timescale of the simulation and problems of large temperature fluctuations for these small system sizes, where differences of 10–20 degrees in temperature will affect the structural comparisons with room temperature experimental data.[2]

The computational cost of dynamics generated with CPMD and the evaluation of the full electronic charge distribution are too prohibitive for the present study. To make these calculations more feasible for the large number of experiments considered here, we have repeated the calculation using the 64-water CPMD trajectory and a *superposition* of DFT molecular densities as an approximation to the full electronic density.

Fig. 5a shows that this approximation is extremely good for liquid water, and provides significant computational savings for the analysis.

Furthermore, there is no need to employ the computationally more expensive BLYP functional any longer since the charge distribution of an isolated water molecule is already well described by the LDA functional as shown in Fig. 5b, where the DFT-BLYP and the DFT-LDA results for an isolated water molecule are compared to recent accurate configuration interaction calculations that included single and double excitations (CISD)[27] which are also in good agreement with coupled cluster calculations (CCSD).[28] All the Quickstep calculations presented in this work used a double-zeta valence plus p polarization (DZVP) and a triple-zeta plus d polarization basis set (TZVP) for H and O, respectively.

We also provide an alternative examination of classical water force fields by using them as the propagators of nuclear positions, and gathering snapshots of the condensed phase trajectories upon which we evaluate intensities based on molecular densities generated using DFT-LDA and eqn. (1). The classical force fields provide us with a much less expensive way to simulate much longer trajectories and larger system sizes while still simulating the intensity curve to make direct contact to the experimental observable.

We calculated $I(Q)$ reported in the Results section using 1-ns-long MD trajectories generated with the classical water models TIP4P[23] and TIP5P[24] for a liquid water model system with 256 water molecules in a simple cubic box, and we used Ewald sums to treat long-ranged electrostatics. 1000 atomic configurations equally spaced by 1 ps were extracted from each trajectory and the corresponding intensity curves were calculated for each atomic configuration. We also calculated $I(Q)$ using eqn. (1) using Monte-Carlo (MC) simulations with the TIP4P-Pol1 and the TIP4P-Pol2 water models,[25] which are polarizable versions of the TIP4P model. In total 1 000 000 MC cycles were performed during each MC simulation and after every 1000 MC cycles an atomic configuration was obtained. Each MC cycle consisted of 500 MC steps to ensure a comparable statistic with respect to the MD simulations.

Results

Figs. 6a–6c show the experimental intensity, with error bars, for representative temperatures of 2 °C, 25 °C, and 77 °C, compared to X-ray scattering data reported by Narten over 30 years ago. The ALS data for these temperatures, and additional temperatures of 10 °C, 44 °C, 55 °C, and 66 °C, are provided in tabular form in the appendix. It is apparent that the ALS X-ray scattering intensities are *qualitatively* different in trend with respect to maximum intensity (I_{max}) over this temperature range, compared to the older X-ray experiments, and the difference between them falls well outside of the ALS experimental error bars. Given the improvements in experimental design such as using a bright and highly monochromatic source, a well-characterized polarization and Compton scattering correction, and more accurate intensities using a modern charge coupled device (CCD) detector, we are confident that the ALS results are more correct. Considering only the ALS data, the features that most prominently change as a function of increasing temperature include decreasing I_{max}, the shifting of the position of the main diffraction peak to higher Q, and the "melting" of the shoulder/peak in the region of 2.5 Å$^{-1} < Q < 3.5$ Å^{-1}.

It is typical practice for water scattering experiments to report radial distributions in addition to the intensity profile, especially since experimental measures of water structure are very important in validating empirical water force fields that describe water structure in terms of real-space distribution
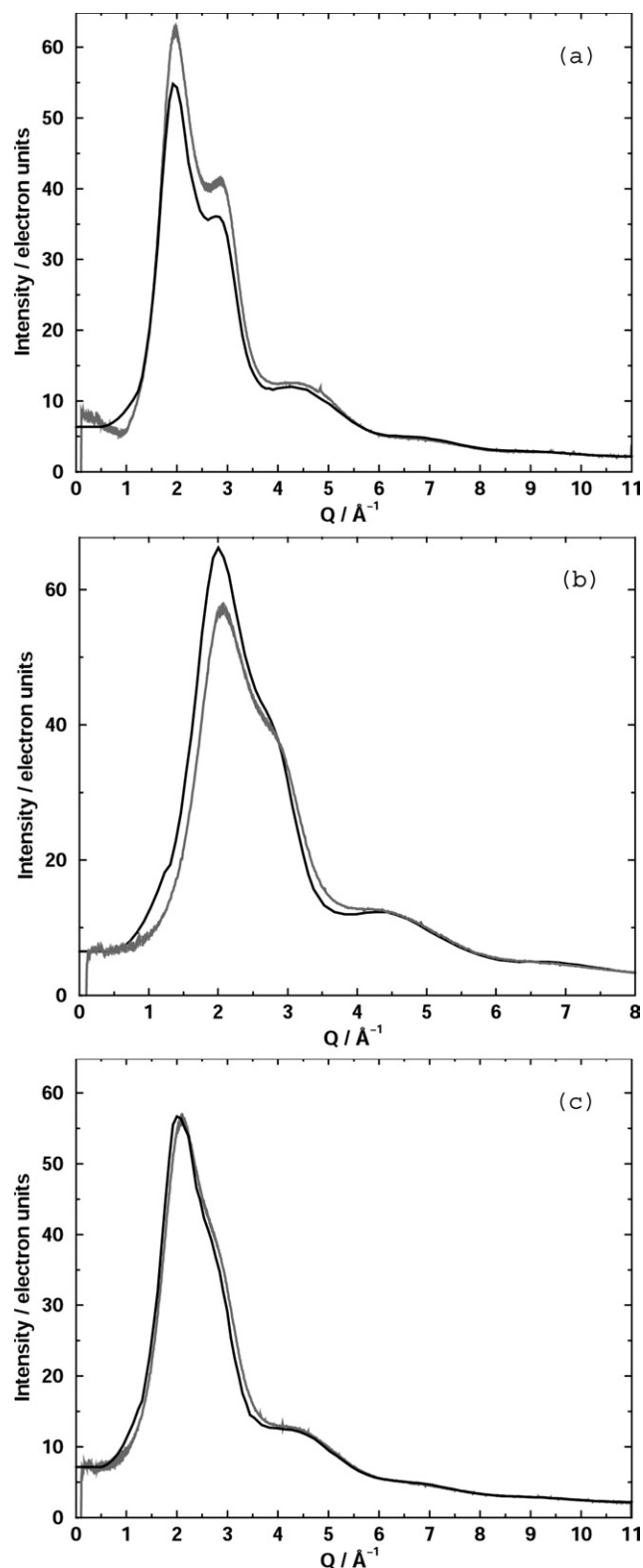
of the $g_{OO}(r)$'s based on finite Q data.[3] Therefore we only report experimental intensity curves in Q-space.

However, we can provide some judgment of the quality of various classical force water models using eqn. (1), where DFT-LDA is used to evaluate the electron density of liquid water based on configurations generated with classical dynamics of a series of empirical water models at various state points. If the simulated intensity curve agrees well with experiment then we can analyze the corresponding real-space functions. In this work we judge the quality of various TIP non-polarizable and polarizable water force fields over the range of temperature of 2–77 °C that we have examined experimentally.

Figs. 7–9 provides a comparison of the experimental intensity data at the state point of 1 bar/25 °C (Fig. 7), 1 bar/2–4 °C (Fig. 8), and 1 bar/75 °C (Fig. 9) with simulated intensities generated with eqn. (1) and DFT-LDA densities, using configurations generated with the non-polarizable TIP4P and TIP5P models, and the polarizable TIP4P-Pol1 and TIP4P-Pol2 water models. We begin by using the position of the main peak and shape of the shoulder region over the temperature range to qualitatively evaluate the models over the temperature range studied.

In Fig. 7 we see that TIP4P reproduces the position of the peak shoulder, but the shoulder is too soft. TIP5P and TIP4P-Pol1 shift the main peak slightly, with slightly better agreement in the shoulder. The best agreement with the experimental intensity is patently obvious for TIP4P-Pol2 model, and shows almost quantitative agreement over the whole curve. For the non-ambient state point at 1 bar/2–4 °C (Fig. 8), close to the temperature of the density maximum of water, the primary feature to note is that the shoulder at room temperature has evolved to a well-defined peak in the experimental intensity. The TIP4P model does not capture the presence of the second peak, and moreover, the main peak height is underestimated. TIP5P and TIP4P-Pol1 show a shifted main peak, but the second peak is well reproduced by both models. TIP4P-Pol2 realizes better agreement with the position of the main peak and very good agreement over the whole intensity curve. At the higher temperature state point of 1 bar/75 °C (Fig. 9), we see a melting of the shoulder/second peak as determined from experiment. All models capture this melting reasonably well, although TIP4P and TIP4P-Pol1 still show a small amount of over-structuring near the shoulder region. TIP5P and TIP4P-Pol2 show similar performance and good agreement with experiment over most of the curve.

Quantitatively, we have defined experimental error bars as low as 1% for some regions of the intensity curve, and an average error of ~2.5% over the range of 0.1 Å^{-1} < Q < 10.0 Å^{-1}. In Table 2 we report chi-squared values for measuring agreement between simulated and experimental intensities over this Q-range, and judge the quality of a model based on not exceeding the 2.5% upper bound in average error. We see from Table 2 that the TIP4P-Pol2 model is quantitatively accurate over the temperature range studied, and therefore we fully endorse its structural properties as being the best among the four models. TIP4P and TIP5P are quantitatively sound for 25 °C and above, but fall outside our accepted error bars for the 4 °C data, although small changes for the better would not be surprising if the simulation were rerun at 2 °C at which the experimental data was collected. TIP4P-Pol1 seems to systematically fail by this quantitative measure throughout the entire temperature range.

Given this level of performance of the simulated intensities using the TIP4P-Pol2 trajectory and DFT-LDA intensities, we can analyze the radial distribution functions generated from the real-space trajectories themselves. Fig. 10 shows the oxygen–oxygen radial distribution functions for TIP4P-Pol2 over the temperature range analyzed here. In our previous theoretical analysis, we concluded that peak position values
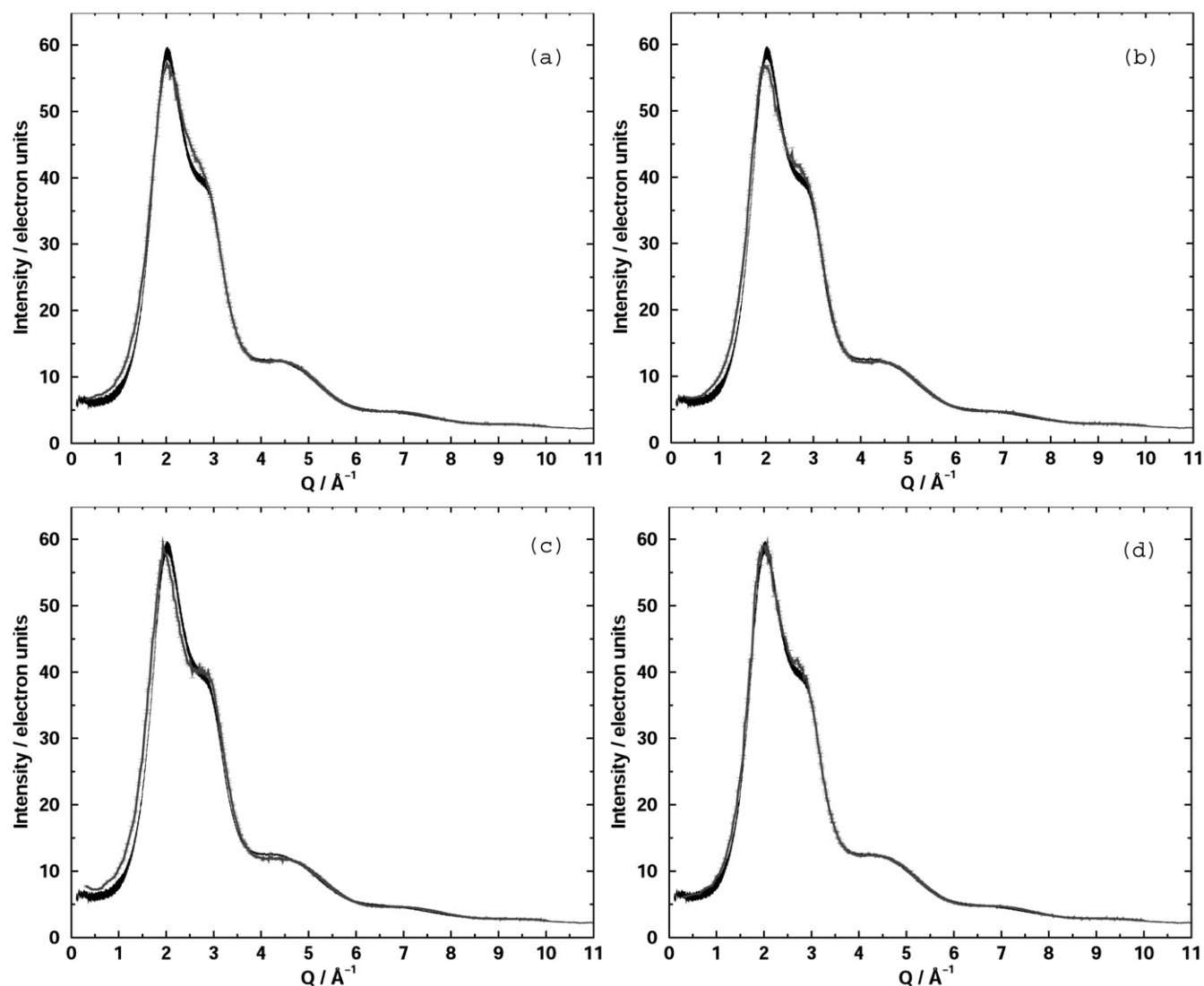

Fig. 6 A comparison of ALS experiment (gray line) and older X-ray experiments (black line). (a) Narten 4 °C, ALS 2 °C. (b) Narten 50 °C, ALS 44 °C. (c) Narten 75 °C, ALS 77 °C.

functions. In our previous study, we introduced a procedure that combines real-space functions to find the optimal $g_{OO}(r)$ which best fits the experimental data.[2] While we believe the independent convergence to the same radial distribution function for ambient conditions by several techniques ensures that the reported ambient $g_{OO}(r)$ is sound (as will be shown later), we break from this tradition here because in actuality there is no way of quantifying the errors introduced in the extraction

Fig. 7 Comparison of experimental spectrum at 27 °C (black line) with simulated X-ray scattering intensities at 25 °C calculated with QUICK-STEP and using trajectory data from a 1-ns-long simulation of 256 water molecules (gray line). (a) TIP4P, (b) TIP5P, (c) TIP4P-Pol1, and (d) TIP4P-Pol2.

of $g_{OO}(r)$ for 25 °C should be reproducible to within 1%, and that a sharper first peak with a *lower bound* in height of 2.6–2.8, best reproduced our ALS2000 experimental data. The current experiments and theoretical models examined here continue to support those results, and further strengthen the finality of the results at room temperature. It is apparent that the trend in the radial distribution functions as a function of temperature is a very structured $g_{OO}(r)$, with sharp peaks and troughs at low temperatures, which melt at higher temperatures. Evidence of tetrahedral bonding at the highest temperatures is found in the still well-defined second peak. The rather good quantitative results between the TIP4P-Pol2 and experimental intensities make these $g_{OO}(r)$'s the current best benchmark for real-space water structure.

The direct calculation of X-ray scattering spectra using *ab-initio* density functional theory based on configurations generated from empirical water force fields provides an alternative way to realize real-space pair correlation functions from the experimental scattering. However, it is important to quantify the relative error introduced by DFT-LDA electron densities *vs.* error in water force fields introduced through the water configurations. Another consideration is the considerable computational cost of evaluating the intensity using eqn. (1) for the

~40 known water models over the temperature range studied here.

We can fortunately examine these questions by comparing to an alternative approach of generating intensities using the MAFFs discussed in the Methods section and eqn. (5). Fig. 11 shows a comparison of intensities derived from DFT-LDA and MAFFs, based on nuclear positions generated with the TIP5P water model (and Ewald electrostatics), to see which approximation agrees better with experiment at 25 °C. We conclude from Fig. 11 that there are small errors in DFT-LDA densities for small Q with respect to experiment, although regions from $3.5 \text{ Å}^{-1} < Q < 5.0 \text{ Å}^{-1}$ are better using DFT-LDA. Therefore disagreement seen at low Q in Figs. 6–8 may involve the LDA functional, DFT, or lack of nuclear quantum effects. Overall the densities by DFT-LDA are robust, with the primary error residing in the configurations generated using the underlying classical force fields. We should also emphasize that we have no evidence that configurations generated by DFT dynamics would improve upon this situation.

Given the comparable quality of intensities generated with MAFFs *vs.* DFT-LDA, we can screen potentially worthwhile water models by first considering their simulated intensity curves using MAFFs against experiment, before proceeding
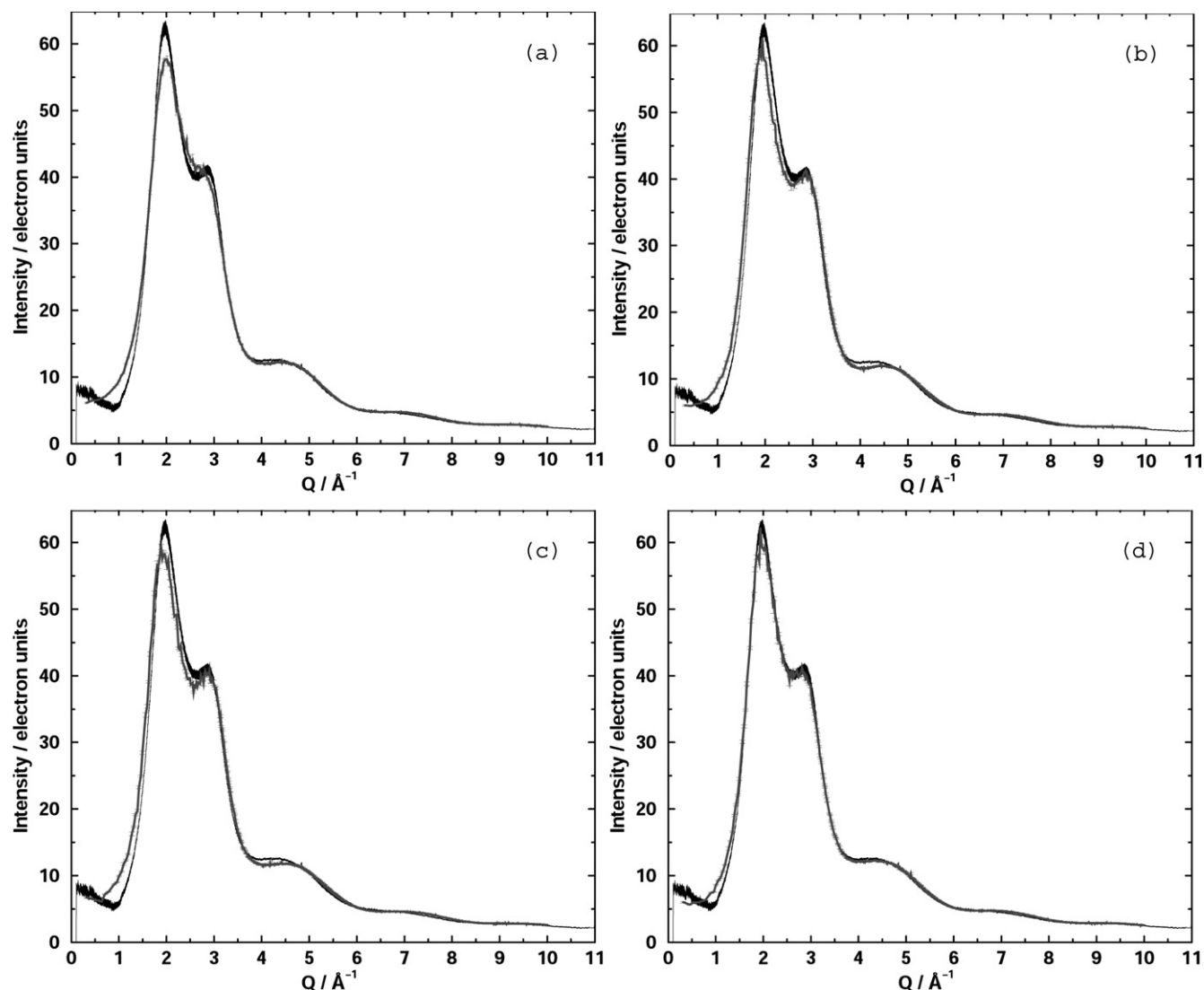
Fig. 8 Comparison of experimental spectrum at 2 °C (black line) with simulated X-ray scattering intensities at 4 °C calculated with QUICKSTEP and using trajectory data from a 1-ns-long simulation of 256 water molecules (gray line). (a) TIP4P, (b) TIP5P, (c) TIP4P-Pol1, and (d) TIP4P-Pol2.

to the more expensive DFT-LDA calculations. Table 3 uses the MAFF analysis to generate percentage error differences for the four models studied here, and various other models including CC,[39] MCY,[40] NCC-vib,[41] SPC,[42] SPC/E,[43] TIP3P,[23] TIP-FQ,[44] ST2,[45] and ST4.[46] The MAFF analysis provides an inexpensive filter to assess the promise of various empirical water force fields for reproducing experiment over the range of temperatures examined here.

Conclusion

We have presented new X-ray scattering data for pure water over a temperature range from 2–77 °C collected at ALS on beam line 7.3.3, which includes the important state point region near the temperature of the density maximum. The ALS X-ray scattering intensities are *qualitatively* different in trend over this temperature range compared to the older X-ray experiments, and fall well outside of the ALS experimental error bars.

The common procedure in the field of water structure is to report both the intensity curve (or structure factor) and an "extraction" of the real-space pair correlation functions from the experimental scattering. While we have a good measure of error in the resulting intensity curve, we have no real definition

of error in the resulting real-space functions due to uncertainty introduced in the experimental corrections, the proper weighting of OO, OH, and HH contributions, and numerical problems of Fourier transforming truncated data in Q-space. For the first time we report the direct calculation of X-ray scattering spectra using *ab-initio* density functional theory. The simulation of the experimental intensity is therefore definitive for determining radial distribution functions over a smaller Q-range.

The *ab initio* simulations are still too expensive to generate adequate statistics for simulating the intensity, and no firm conclusions can yet be drawn as to the adequacy of DFT dynamics. Instead, DFT with the LDA functional was used to evaluate the electron density of liquid water based on configurations generated with classical dynamics of a series of empirical water models at various conditions, including TIP4P, TIP5P, TIP4P-Pol1 and TIP4P-Pol2.

The experimental and theoretical benchmarks of intensity data provide a means for measuring the progress made in the modeling of water structure. The series of TIPnP non-polarizable models have shown continuous improvement over the years, and the most recent TIP5P model has exhibited excellent agreement with the experiment at room temperature reported in 2000,[2,3] and which has been confirmed again here. Many research groups have actively acknowledged this
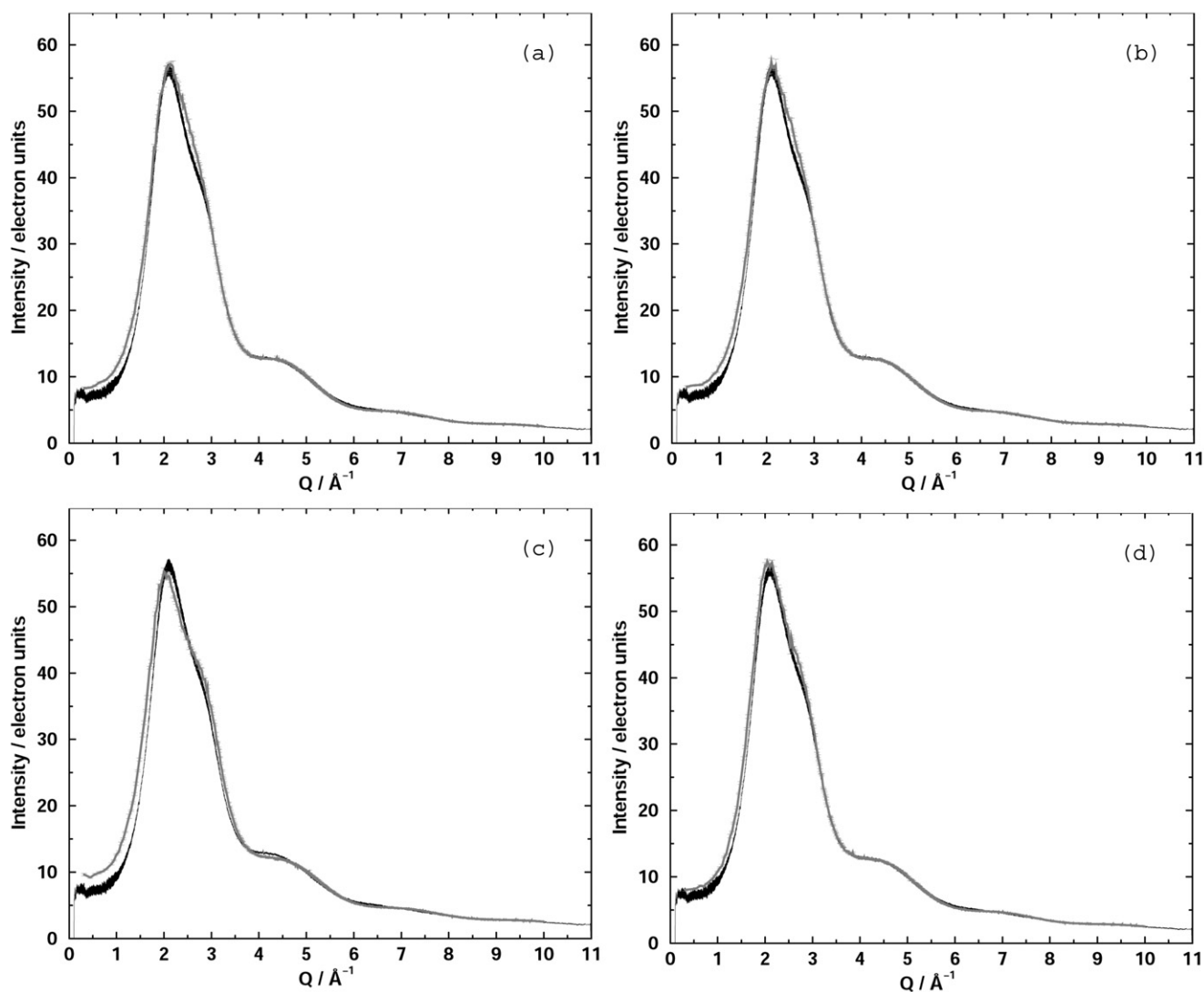
Fig. 9 Comparison of experimental spectrum at 75 °C (black line) with simulated X-ray scattering intensities at 77 °C calculated with QUICK-STEP and using trajectory data from a 1-ns-long simulation of 256 water molecules (gray line). (a) TIP4P, (b) TIP5P, (c) TIP4P-Pol1, and (d) TIP4P-Pol2.

progress by adopting TIP5P in application to the liquid–liquid phase transition in water[47,48] and disseminating the model in molecular mechanics programs.[49,50] We note that quantitative agreement is not adequate at 4 °C, although further analysis may be required in regard to treatment of long-ranged electrostatics and simulating with the temperature fixed to the experimental value of 2 °C. We do find that the TIP5P model simulated without Ewald, consistent with the Jorgensen protocol,[24] does perform better than the model simulated with Ewald treatment of long-ranged electrostatics (see Table 3).

We also focused on the TIP4P-Pol polarizable models developed by Chen and co-workers[25] based on fluctuating charge models,[25,44,51,52] which allow for significant shifts of electron

density from one atom to surrounding atoms or bonds within the same molecule. The approach adopted in ref. 25 fits to properties of the liquid phase at ambient conditions and to properties of gas-phase monomers and clusters, with the reasoning that fitting to two different thermodynamic states (with respect to density) should also yield a good description for other densities. We found impressive quantitative agreement with experiment over the whole temperature range from 2–77 °C for the TIP4P-Pol2 model, and it provides the current best benchmark for radial distribution functions over this temperature range.

Given the comparable quality of intensities generated with MAFFs *vs.* DFT-LDA, we can screen potentially worthwhile water models by first considering their simulated intensity curves using MAFFs against experiment, before proceeding to the more expensive DFT-LDA calculations. In fact, the TIP4P-Pol2 model was chosen for further study with DFT-LDA because of pre-screening with the MAFF approach. While it might be argued that the MAFF analysis provides an equally good, but less expensive, approach to DFT-LDA (even with the further approximation of molecular superposition) for evaluating simulation intensities, we see these approaches as mutually beneficial. Ultimately first principles approaches will be more generally applicable, although expensive. MAFFs would be preferred based on reduced
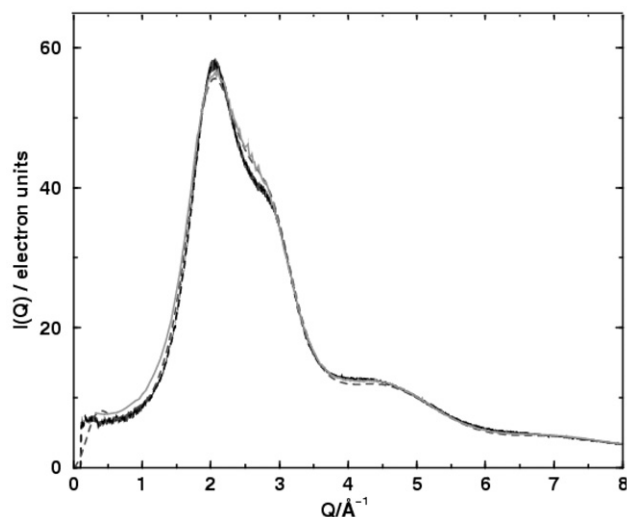
Table 2 Percentage difference between experimental and simulated intensities using DFT-LDA over the Q-range of 0.4–10.0 Å^{-1} at three different temperatures for different empirical water models

Temperature/°C	TIP4P	TIP5P	TIP4P-Pol1	TIP4P-Pol2
2	3.3%	4.7%	5.8%	1.8%
25	1.8%	2.2%	4.4%	1.0%
75	2.2%	2.0%	5.5%	1.7%
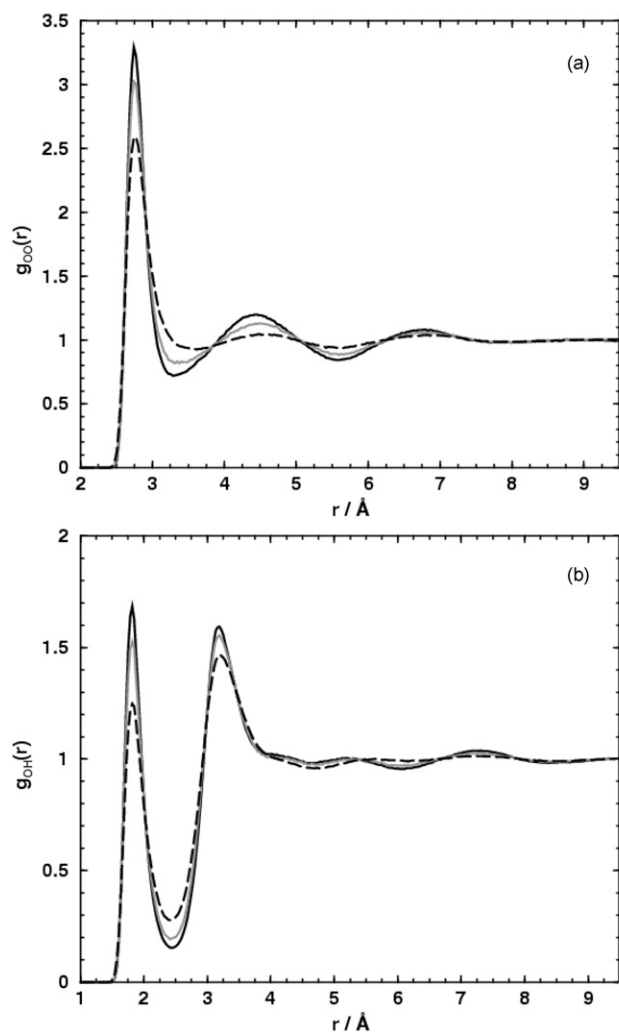
Fig. 10 Real-space distribution functions from the TIP4P-Pol2 model that best reproduces the experimental intensity for 2 °C (black), 25 °C (gray), and 77 °C (dashed). (a) $g_{OO}(r)$, and (b) $g_{OH}(r)$.

computational expense and comparable accuracy, but would require a refitting of parameters at greater extremes of temperature and pressure, and require extension to other molecules and heterogeneous solutions.

Fig. 11 Comparison of DFT-LDA and MAFF's using the same underlying real-space trajectory for reproducing the experimental intensity.

Table 3 Percentage difference between experimental and simulated intensities using MAFFs over the Q-range of 0.4–10.0 Å^{-1} at three different temperatures for different empirical water models

Water model	2 °C	25 °C	77 °C
CC		5.3%	
MCY		11.5%	
NCC-vib		6.2%	
SPC		2.0%	
SPC/E	2.8%	1.7%	1.8%
TIP3P		4.2%	
TIP4P		1.0%	
TIP5P (no Ewald)		3.5%	
TIP5P (Ewald)	3.8%	5.8%	1.4%
TIP4P-Pol1	3.7%	3.5%	3.2%
TIP4P-Pol2	1.2%	0.9%	1.7%
TIPAB		4.3%	
ST2	8.3%	7.9%	6.3%
ST4		5.0%	

Acknowledgements

References

1 G. Hura, J. M. Sorenson, R. M. Glaeser and T. Head-Gordon, *J. Chem. Phys.*, 2000, **V113**, 9140–9148.
2 J. M. Sorenson, G. Hura, R. M. Glaeser and T. Head-Gordon, *J. Chem. Phys.*, 2000, **V113**, 9149–9161.
3 T. Head-Gordon and G. Hura, *Chem. Rev.*, 2002, **V102**, 2651–2669.
4 A. H. Narten and H. A. Levy, *J. Chem. Phys.*, 1971, **55**, 2263–2269.
5 A. H. Narten and H. A. Levy, in *Water A Comprehensive Treatise*, ed. F. Franks, Plenum Press, New York, 1972, vol. 1, pp. 311–332.
6 A. H. Narten and W. E. Thiessen, *Science (Washington, D. C.)*, 1982, **217**, 1033–1034.
7 A. H. Narten, C. G. Venkatesh and S. A. Rice, *J. Chem. Phys.*, 1976, **64**, 1106–1121.
8 A. K. Soper and R. N. Silver, *Phys. Rev. Lett.*, 1982, **49**, 471–474.
9 Y. E. Gorbaty and Y. N. Demianets, *Mol. Phys.*, 1985, **55**, 571–588.
10 A. K. Soper and M. G. Phillips, *Chem. Phys.*, 1986, **107**, 47–60.
11 J. C. Dore, in *Hydrogen Bond Physics International Conference*, Barga, Italy, 1991, pp. 193–211.
12 A. K. Soper, F. Bruni and M. A. Ricci, *J. Chem. Phys.*, 1997, **V106**, 247–254.
13 J. Dore, *Chem. Phys.*, 2000, **V258**, 327–347.
14 A. K. Soper, *Chem. Phys.*, 2000, **V258**, 121–137.
15 A. K. Soper, *Chem. Phys.*, 1996, **202**, 295–306.
16 R. L. McGreevy and L. Puszati, *Mol. Simul.*, 1988, **1**, 359.
17 R. L. McGreevy, *Nuclear Instruments & Methods in Physics Research Section a-Accelerators Spectrometers Detectors and Associated Equipment*, 1995, **V354**, 1–16.
18 R. Car and M. Parrinello, *Phys. Rev. Lett.*, 1985, **55**, 2471–2474.
19 M. Sprik, J. Hutter and M. Parrinello, *J. Chem. Phys.*, 1996, **V105**, 1142–1152.
20 P. L. Silvestrelli and M. Parrinello, *J. Chem. Phys.*, 1999, **V111**, 3572–3580.
21 E. Schwegler, G. Galli and F. Gygi, *Phys. Rev. Lett.*, 2000, **V84**, 2429–2432.
22 M. Krack, A. Gambirasio and M. Parrinello, *J. Chem. Phys.*, 2002, **V117**, 9409–9412.
23 W. L. Jorgensen, J. Chandrasekhar, J. D. Madura, R. W. Impey and M. L. Klein, *J. Chem. Phys.*, 1983, **79**, 926–935.
24 M. W. Mahoney and W. L. Jorgensen, *J. Chem. Phys.*, 2000, **V112**, 8910–8922.

25 B. Chen, J. H. Xing and J. I. Siepmann, *J. Phys. Chem. B*, 2000, **V104**, 2391–2401.
26 B. L. Henke, E. M. Gullikson and J. C. Davis, *At. Data Nucl. Data Tables*, 1993, **V55**, 349.
27 J. H. Wang, A. N. Tripathi and V. H. Smith, *J. Chem. Phys.*, 1994, **V101**, 4842–4854.
28 N. Watanabe, S. Ten-no, S. Pal, S. Iwata and Y. Udagawa, *J. Chem. Phys.*, 1999, **V111**, 827–832.
29 J. Krogh-Moe, *Acta Crystallogr.*, 1956, **9**, 951.
30 N. Norman, *Acta Crystallogr.*, 1957, **10**, 370.
31 A. Rahman and F. H. Stillinger, *J. Am. Chem. Soc.*, 1973, **95**, 7943–7948.
32 S. Izvekov and G. A. Voth, *J. Chem. Phys.*, 2002, **V116**, 10 372–10 376.
33 C. Lee, W. Yang and R. G. Parr, *Phys. Rev. B*, 1988, **37**, 785.
34 A. D. Becke, *Phys. Rev. A*, 1988, **38**, 3098–3100.
35 B. Miehlich, A. Savin, H. Stoll and H. Preuss, *Chem. Phys. Lett.*, 1989, **157**, 200.
36 J. P. Perdew, K. Burke and M. Ernzerhof, *Phys. Rev. Lett.*, 1996, **V77**, 3865–3868.
37 G. Lippert, J. Hutter and M. Parrinello, *Theor. Chem. Acc.*, 1999, **103**, 124–140.
38 M. Krack and M. Parrinello, *Phys. Chem. Chem. Phys.*, 2000, **2**, 2105–2112.
39 A. A. Chialvo and P. T. Cummings, *J. Chem. Phys.*, 1996, **V105**, 8274–8281.
40 O. Matsuoka, E. Clementi and M. Yoshimine, *J. Chem. Phys.*, 1976, **64**, 1351.
41 G. Corongiu and E. Clementi, *J. Chem. Phys.*, 1992, **V97**, 2030–2038.
42 H. Berendsen, J. Postma, W. F. van Gunsteren and J. Hermans in *Intermolecular forces: proceedings of the Fourteenth Jerusalem Symposium on Quantum Chemistry and Biochemistry*, ed. B. Pullman and D. Reidel, sold and distributed in the USA and Canada by Kluwer, Boston, 1981, ix, 567, vol. 14.
43 H. J. C. Berendsen, J. R. Grigera and T. P. Straatsma, *J. Phys. Chem.*, 1987, **91**, 6269–6271.
44 Y. P. Liu, K. Kim, B. J. Berne, R. A. Friesner and S. W. Rick, *J. Chem. Phys.*, 1998, **V108**, 4739–4755.
45 A. Rahman and F. Stillinger, *J. Chem. Phys.*, 1971, **55**, 3336.
46 T. Head-Gordon and F. H. Stillinger, *J. Chem. Phys.*, 1993, **V98**, 3313–3327.
47 M. Yamada, S. Mossa, H. E. Stanley and F. Sciortino, *Phys. Rev. Lett.*, 2002, **V8819**, U119–U122.
48 H. E. Stanley, M. C. Barbosa, S. Mossa, P. A. Netz, F. Sciortino, F. W. Starr and M. Yamada, *Physica A (Amsterdam)*, 2002, **V315**, 281–289.
49 E. Lindahl, B. Hess and D. van der Spoel, *J. Mol. Model.*, 2001, **V7**, 306–317.
50 D. A. Pearlman, D. A. Case, J. W. Caldwell, W. S. Ross, T. E. Cheatham, S. Debolt, D. Ferguson, G. Seibel and P. Kollman, *Comp. Phys. Commun.*, 1995, **V91**, 1–41.
51 S. W. Rick, S. J. Stuart and B. J. Berne, *J. Chem. Phys.*, 1994, **V101**, 6141–6156.
52 S. W. Rick, *J. Chem. Phys.*, 2001, **V114**, 2276–2283.